Evolution of secondary vorticity following vortex ring impact on a concave hemicylindrical cavity ⊘

T. Ahmed ⓘ ; B. D. Erath ✉ ⓘ

Check for updates

CHORUS

View Online

Export Citation

Articles You May Be Interested In

Prosodic differences in tracheoesophageal speech: Perception and production

J Acoust Soc Am (November 2001)

An experimental model for the study of tracheoesophageal phonation

J Acoust Soc Am (April 2022)

Replacing tracheoesophageal voicing sources using LPC synthesis

J Acoust Soc Am (September 1990)

Evolution of secondary vorticity following vortex ring impact on a concave hemicylindrical cavity

View Online   Export Citation   CrossMark

T. Ahmed[1] (iD) and B. D. Erath[1,2,a] (iD)

AFFILIATIONS

[1]Department of Mechanical & Aerospace Engineering, Clarkson University, Potsdam, New York 13699, USA
[2]Department of Mechanical Engineering, Rochester Institute of Technology, Rochester, New York, 14623, USA

[a]Author to whom correspondence should be addressed: bdeeme@rit.edu

ABSTRACT

The generation of secondary vortices from a wall-bounded vorticity sheet is a frequent occurrence in vortex ring–structure interactions. Such interactions arise in both engineering and biomedical applications, including tracheoesophageal speech. This study investigated the evolution of secondary vorticity following impact of an axisymmetric vortex ring on a concave hemicylindrical cavity. A primary vortex ring (PVR) with a formation number of $F = 2.00$ and Reynolds number of $Re_\Gamma = 1500$ was generated within a water tank. Five different ratios of hemi-cylindrical cavity radius (R_{cyl}) to PVR radius (R_v) were examined; namely, $\gamma = 4$, 3, $2\frac{1}{2}$, 2, and $1\frac{1}{2}$. Flow visualization and particle image velocimetry analysis of the scenarios revealed the asymmetric impact of the PVR on the cavity surface. This asymmetric impact leads to distinctive flow dynamics in the evolution of secondary vorticity across both the transverse and longitudinal planes. In the transverse plane, the PVR impact generated a secondary vortex ring (SVR) and a tertiary vortex ring (TVR). Following generation, the SVR and TVR rotated completely around the PVR. In the longitudinal plane, the SVR produced a horseshoe-like loop instead of rotating around the PVR completely. For $\gamma = 4$, 3, and $2\frac{1}{2}$, the SVR loop moved upward due to self-induction. For $\gamma = 2$ and $1\frac{1}{2}$, the legs of the SVR horseshoe-like loop experienced reconnection and produced two new vortex rings. The upward trajectory of the SVR horseshoe-like loop varied with γ, tending to move further from the primary ring's axis as γ decreased.

I. INTRODUCTION

Scenarios that give rise to vortex laden flows interacting with a boundary are ubiquitous, and span applications that range from engineering[1–7] to biological flows.[8–12] One of the most common vortex structure interactions is a vortex ring impinging on a solid boundary, where prior work has shown that both the geometry of the structure, and the orientation of the vortex ring relative to it, influence the resultant collision dynamics.[3,4,7,11]

The impact of an axisymmetric vortex ring on a surface is a highly researched area within the broader field of fluid–structure interactions.[13–25] The simplest configuration is an axisymmetric vortex ring impinging normally on a flat wall such that an axisymmetric collision is produced.[13–17,20] The dynamics of this interaction are dependent on the Reynolds number of the primary vortex ring (PVR), which can be defined as $Re_\Gamma = \Gamma/\nu$, where Γ is the vortex ring circulation, and ν is the kinematic viscosity of the fluid medium. At very low Reynolds numbers ($Re_\Gamma < 250$), viscous dissipation dominates the interaction and no additional flow structures are produced.[14,26,27] For moderate Reynolds numbers, as the PVR approaches the wall it induces the formation of a secondary vortex ring (SVR) from the wall-bounded vorticity. If Re_Γ is high enough, a tertiary vortex ring (TVR) may also be produced.[13,14,16,28,29] Following formation, both the secondary and tertiary rings subsequently orbit the primary ring and are ultimately entrained into the core of the PVR. For sufficiently high Reynolds Numbers ($Re_\Gamma > 2800$), instead of orbiting the PVR, the SVR advects upward and away from the impact surface.[17,30] This behavior can be induced at lower Reynolds numbers by changing the surface of contact from a flat plate to a hemispherical cavity.[31] That is, the surface geometry can be manipulated to more efficiently transfer vorticity from the PVR to the SVR.

In some scenarios, the entire circumference of the vortex ring may not simultaneously come into contact with a surface during collision; this is referred to herein as an "asymmetric" impact. This interaction can occur when the trajectory of a vortex ring is oriented at an acute angle relative to the wall, or when the vortex ring itself has an initial non-circular shape. Because this study focuses on circular vortex ring interactions, subsequent references to asymmetric impact will refer to the specific case of a circular vortex ring impacting a surface in
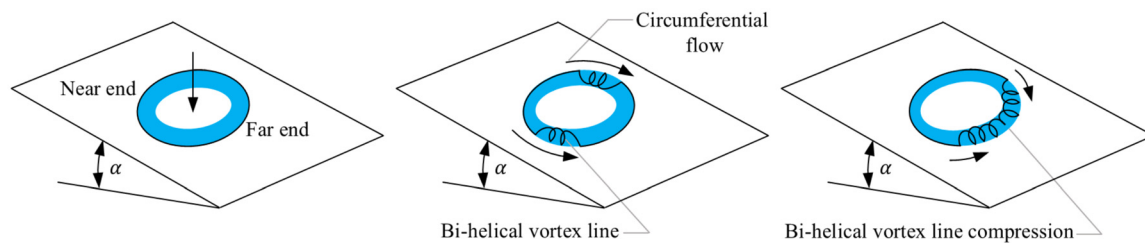
22 January 2025 15:56:32

FIG. 1. Schematic diagram of an asymmetric vortex ring impacting an inclined surface, and the subsequent formation of bi-helical vortex lines, as identified by Lim.[32]

a nonuniform manner. Figure 1 schematically represents the asymmetric impact of a circular vortex ring on a flat wall that is oriented at an acute angle (α) relative to the direction of vortex ring advection. The progression in time is shown from left to right. The first portion of the vortex ring that comes into contact with the wall is referred to as the "near end" while the opposite side is referred to as the "far end" (see Fig. 1).[20,28,32–36]

During asymmetric interactions the PVR experiences non-uniform stretching,[32,34] which is more pronounced at the near end than the far end. The variable stretching rate of the PVR leads to the formation of bi-helical vortex lines along the core of the PVR (see Fig. 1). Inducement of the SVR (not graphically presented in Fig. 1) at the boundary initially occurs at the near end before progressing to the far end. Orbiting of the SVR around the PVR progresses in a similarly delayed fashion.[32] As the SVR orbits the PVR it induces circumferential flow along the core of the PVR (see Fig. 1), which compresses the bi-helical vortex lines toward the far end of the ring (see Fig. 1). This, in turn, increases the PVR core diameter at the far end and pushes the PVR away from the line of symmetry.[27,32,34] As the interaction progresses, cross-sign vorticity interactions between the PVR and SVR at the near end lead to rapid annihilation of vorticity. At the far end the SVR produced by the PVR is characterized by an increasing core diameter, relative to the near end, because vorticity diffusion is decreased in this region.[28,32] Consequently, as the SVR orbits the PVR a horseshoe-like loop is produced at the far end, which advects away from the vicinity of the wall due to mutual induction between the legs.[28,32] The trajectory of this upward moving horseshoe-like loop appears to depend on the angle with which the PVR is initially oriented relative to the wall, although this aspect of the interaction remains unexplored.[34]

A variety of biological and engineering scenarios are characterized by the more complex scenario of a vortex ring asymmetrically impacting a concave cavity.[3,11,37] A problem of particular interest arises during the production of replacement speech via tracheoesophageal speech (TES). In individuals that have undergone a laryngectomy, TES is produced by placing a prosthesis in the posterior wall of the trachea that acts as a shunt and redirects airflow from the trachea into the esophagus. The success of TES depends on the size and orientation of this prosthesis relative to the esophagus,[38] as the subsequent flow field that develops in the esophagus is what ultimately produces TES. During TES vortex rings are generated at the exit of the prosthesis before entering the cylindrical-shaped geometry of the esophagus where they subsequently impinge on the posterior (back wall).[11]

This, and similar scenarios, have motivated fundamental studies of vortex-ring cavity flow interactions, including a vortex ring impinging on a concave hemicylindrical cavity[39] and a vortex ring impacting

a V-wall. The latter configuration can essentially be treated as two individual inclined-walls symmetrically joined at the apex.[35] In both of these scenarios, despite the vortex ring being oriented normal to the trough of the cavity surface, the ring impacts the surface asymmetrically due to the two-dimensional (2D) geometry of the cavity surface. The resultant flows are characterized by their behavior in two separate planes; one extending in the transverse direction (referred to in prior studies as the concave[39] and valley[35] plane) and the other in the longitudinal direction (previously referred to as the straight edge[39] and orthogonal[35] plane). Note, due to the asymmetric collision that occurs when an axisymmetric vortex ring impacts a 2D concave structure, the mechanics are noticeably different between the two (e.g., transverse and longitudinal) planes.

In the transverse plane, the flow experiences confinement due to the wall boundaries. For a hemicylindrical cavity the PVR impacts the interior wall of the hemicylinder surface in the transverse plane. As the PVR approaches the surfaces of the interior wall in the transverse plane both a SVR and TVR are generated. Both rotate completely around the PVR and the rotational speed increases as the PVR Reynolds number increases.[39] Due to confinement of the PVR by the cavity wall, its diameter does not noticeably increase; in contrast to the longitudinal plane where the unbounded PVR grows significantly in diameter.[39] For the V-wall cavity,[35] the physics of the PVR impacting on the cavity in the transverse plane are similar to those observed for a vortex ring impacting an inclined plate.[32] Specifically, there is high localized vorticity annihilation after the initial generation of the SVR and TVR. However, for the V-wall configuration the rotation of the SVR and TVR around the PVR is accompanied by the PVR cores migrating toward the apex of the V-wall. Circumferential flow and bi-helical vortex lines are also generated in the transverse plane along the core of the primary ring.[35]

For vortex ring–2D cavity interactions, the flow is unbounded in the longitudinal plane, which leads to the development of unique physics. The core diameter of the PVR is much larger in the longitudinal plane than the transverse plane, with less circulation strength. As a result, the SVR does not fully rotate around the PVR in the longitudinal plane and the rotational speed as it orbits the PVR is much less than in the transverse plane. Instead of wrapping around the PVR, the SVR initially moves toward the PVR axis and away from the cavity surface. In tandem with this behavior, the bi-helical vortex lines that are generated in the transverse plane compresses the PVR in the longitudinal plane. This causes the PVR to quickly become incoherent, with a weak tertiary vortex ring generated at the wall.[39]

While the two aforementioned studies[35,39] provide insight into the physics of a vortex ring impacting on a 2D concave cavity, there are important aspects of the interaction that have not been detailed.

22 January 2025 15:56:32

First, the mechanics that lead to the SVR advecting away from the surface are not clear, as unbounded interactions arising from a vortex ring impacting a flat plate at a similar Reynolds numbers produce an SVR that orbits the PVR without being ejected.[15,17]

Possible insight into this behavior can be found by considering the case of a vortex pair impacting a wavy wall, where the vortex lines are oriented in the same direction as the changing wall amplitude.[36] In this scenario, a vortex ring is generated in the valley of the wavy wall. This occurs as the secondary vortex line begins to orbit the primary vortex line before being deformed into a horseshoe-like loop that ultimately pinches off and forms the new ring. This new ring advects away from the wall at 180° from the initial trajectory of the primary vortex pair.

For the current scenario of interest, an axisymmetric vortex ring impacting a 2D hemicylindrical cavity, it is not clear if a new vortex ring is formed in the longitudinal plane, as prior work has only identified that secondary vorticity in the longitudinal plane is ejected away from the wall.[39] Notably, the trajectory (i.e., angle) of the secondary vorticity is also different than that of the vortex ring that is ejected from the valley of the wavy wall. Second, the effect of cavity size has not been fully explored. More specifically, it is not clear how the diameter of the cavity influences the formation and possible ejection of secondary vorticity in the longitudinal plane. This is expected to play a role in the mechanics as changing the cavity diameter will influence the degree of asymmetry that is introduced when the PVR impacts the surface, and prior work exploring axisymemtric interactions with acutely angled flat plates has shown the physics of the secondary vorticity at the far end are influenced by the degree of asymmetry during impact.[34] Furthermore, although the influence of geometry has been explored for vortex ring interactions with a V-wall,[35] this scenario is not directly analogous to TES, which motivates the current work. Namely, a V-wall lacks surface curvature, which has been shown to play an important role in the diffusion of vorticity at the boundary.[31] Hence, a curved hemicylindrical boundary is anticipated to produce different mechanics than a V-wall.[39]

The aim of this study is to elucidate the evolutionary mechanics of secondary vorticity produced by a constant diameter axisymmetric vortex ring impinging normally on a 2D concave hemicylindrical cavity, and explore this interaction as a function of cavity diameter. Both qualitative flow visualization and quantitative particle image velocimetry (PIV) measurements are performed in an experimental facility that uses a piston-cylinder arrangement to generate the primary vortex ring. Section II details the experimental facility, measurements, and methodology. The results are presented and discussed in Secs. III and IV is left for the conclusions.

II. EXPERIMENTAL DESIGN AND METHODOLOGY
A. Facility setup

Figure 2 shows the schematic diagram of the experimental facility. A cylindrical coordinate system is used. The origin of the coordinate system is aligned with the central axis of the vortex tube. The z axis corresponds to the axial direction, running along the length of the vortex tube and points toward the contact surface. The radial direction, r, points outward from the vortex tube axis. In this manuscript, the radial distance in the transverse plane will be denoted as r_t, and in the longitudinal plane as r_l. The azimuthal angle θ defines the angle of rotation around the vortex tube axis. A 5500 cm³ water tank was

employed for all of the investigations. A piston-tube arrangement was used to generate a vortex ring. The clear acrylic vortex tube was 30.48 cm long with an outer diameter of 5.08 cm and a smooth inner diameter of $d_t = 3.80$ cm with a tolerance of ± 0.05 cm. To facilitate the detachment of vorticity the exit was externally chamfered at a 20° angle. A linear actuator, Pololu (LACT12P-12V-05) with a 5:1 gear ratio drove a custom-made 3D printed piston, which employed a circumferential o-ring to ensure an appropriate seal. A Jrk G2 24v13 USB motor controller with feedback was paired with an Arduino Uno to control the speed, U_p, and stroke length, L, of the actuator. An impulse piston velocity program was chosen for the piston movement.[40–42] The mean piston velocity was $U_p = 3.20$ cm/s. The precise time history of the piston velocity profile is available in prior work.[31] A vortex ring with a formation number of $F = L/d_t = 2.00$, and Reynolds number of $Re_\Gamma = \Gamma/\nu \approx 1500$ was generated, where Γ is the vortex ring circulation quantified from velocity field data, and ν is the kinematic viscosity of the water. The formation number ($F = 2.00$) was specifically chosen to prevent the generation of a trailing jet behind the PVR, which could otherwise affect the upward motion of the SVR.

The contact surface consisted of a clear acrylic half cylinder (hemicylinder). Five different hemicylinder radii, R_{cyl}, were employed in the study; namely $R_{cyl} = 20.32$, 15.24, 12.70, 10.16, and 7.62 cm. The ratio of the hemicylinder to PVR radius was expressed as $\gamma = R_{cyl}/R_V \approx 4$, 3, $2\frac{1}{2}$, 2, and $1\frac{1}{2}$. Because R_V was fixed for the experiments, γ decreases with decreasing hemicylinder radius. Additional details regarding the experimental facility can be found in a previous publication.[31]

Both qualitative fluid flow visualization and quantitative planar two-dimensional and tomographic PIV measurements (2D-PIV and tomo-PIV, respectively) were employed to identify the key vortical structures produced during the interaction. Data were acquired in three different planes; namely, transverse and longitudinal planes, and a top view imaged along an axis angled 30° from the of the centerline of the vortex tube. A representation of the three data planes is shown in Fig. 3.

B. Experimental method
1. Qualitative measurements

Dye flow visualization was performed by seeding the vortex tube fluid with a naturally buoyant solution made using blue food dye, isopropyl alcohol, tap water and whole milk. Visualization data were captured from the inclined top plane using a GoPro Hero8 Black camera with a pixel resolution of 1920×1080 pixel. An Arduino Uno was used to obtain synchronization between linear actuator and the camera. Flow visualization images were captured at 100.00 Hz for 35.00 s. The time was nondimensionalized as $\tau = tU_p/d_t$, which corresponds to a range of $0.00 \leq \tau \leq 29.40$, where $\tau = 0.00$ corresponds to the start of the piston movement.

2. Quantitative measurements

2D-PIV measurements were acquired in both the transverse and longitudinal planes. The flow was seeded with Cospheric fluorescent red polyethylene microspheres (995 kg·m⁻³) with a diameter of 65–75 μm. A Litron Nano 532 nm Nd:YAG laser operating at 50 mJ/pulse was used to illuminate the particles (see Fig. 2). A
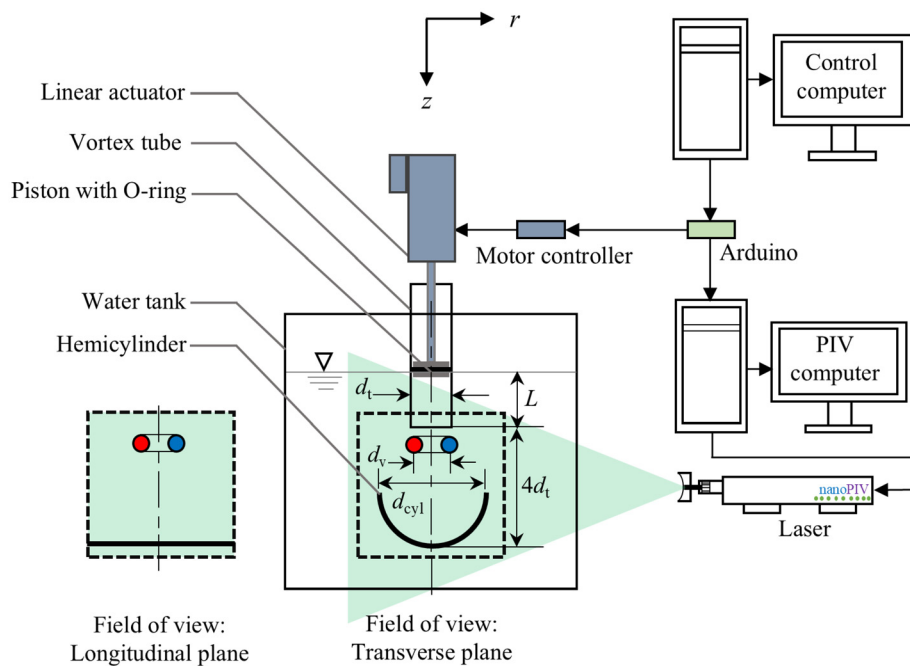
FIG. 2. Schematic diagram of the experimental facility.

LaVision sCMOS camera (2560×2160 pixel) along with a NIKKOR 70 mm lens was positioned perpendicular to the light sheet at a distance of 71 cm. A long pass filter of 550 nm was placed over the camera lens during image acquisition to enhance image signal to noise ratio by eliminating laser light reflections. Image dewarping was employed to correct image distortion caused by the different indices of refraction between the fluid and the acrylic hemicylinder. During data acquisition in the longitudinal plane a dewarping self-calibration was performed to minimize image distortions. This was achieved by imaging a
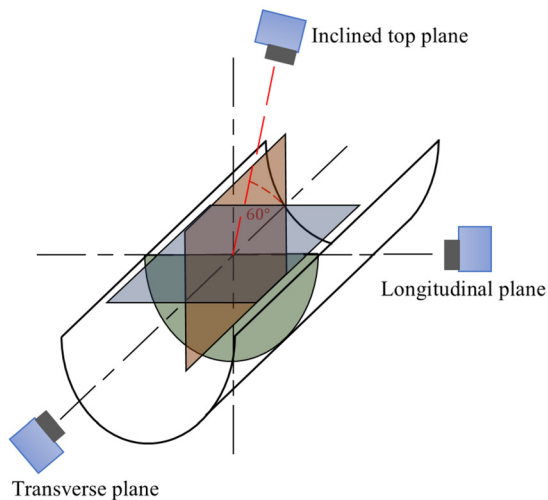

FIG. 3. Schematic diagram representing the data collection planes; namely, the transverse, longitudinal, and inclined top plane, for an axisymmetric vortex ring impinging on a 2D hemicylindrical cavity.

calibration plate at the focal plane (interior to the curved hemicylinder surface) and then applying the dewarping algorithm available in the DaVis software.

Because the total time of interaction was 35 s, PIV data were acquired at discrete intervals to minimize the processing time. Sequential sets of four images were acquired at time intervals of $dt_{set} = 1.0$ s, with the time between each image in a set equal to $dt_{image} = 0.033$ s. All raw images were processed to extract velocity vector fields using DaVis 8.2.2 software from LaVision. A time series, cross correlation scheme with recursive 64×64 pixel and 32×32 pixel interrogation windows with 50% overlap was used to calculate the velocity field from each set of PIV images. The field of view was 22.4×18.8 cm^2, which produced a spatial resolution of 0.14 cm.

No post-processing of the vector fields was performed. This process yielded 35 sets of three time-resolved vector fields as the vortex ring advected though the flow domain. To address flow instabilities and minimize uncertainty, an ensemble-averaged velocity field was calculated at each instance in time from 70 acquisitions. This specific number was selected based on minimizing the root mean square error in comparison to the mean flow field from a substantially large sample size of 980 vector fields. The determination of 70 as the optimal number of averaged velocity fields was based on the value where the error asymptotically approached a stable value of approximately 0.5%. The uncertainty of the 2D velocity field was estimated by accounting for the ability of the particles to follow the flow, as well as the uncertainty in determining the particle displacement. Uncertainty due to particle inertia was estimated to be $\approx$1% because the particles Stokes number was less than 0.1.[43] Errors due to particle sedimentation were found to be 0.14% based on the advection velocity of the vortex ring. Uncertainty due to correlation errors (0.1 pixel)[44] relative to the average particle displacement ($\approx$6 pixel), as well as the error due to the timing uncertainty
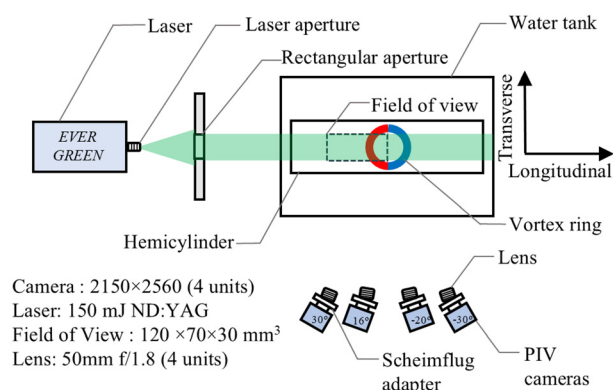
FIG. 4. Schematic of the tomo-PIV orientation in the experimental facility.

resulted in a processing error of 1.68%. Consequently, the total relative uncertainty was estimated to be ≈2.03%.

Tomo-PIV measurements were conducted in a 210 000 cm^3 water tank, using the orientation (longitudinal plane) schematically presented in Fig. 4, with the rest of the facility remaining unchanged. Tomo-PIV data were only acquired for the cases of $\gamma = 3$, 2, and $1\frac{1}{2}$. The measurements were performed using four $16-$bit, 2560×2150 pixel CCD cameras (LaVision ImagerPro X). The cameras were positioned in a linear array on one side of the water tank at angles of $30°$, $16°$, $-20°$, and $-30°$ measured relative to the transverse plane. Each camera had a 50 mm, $f/1.8$ NIKKOR lens. The lenses were mounted onto a Scheimpflug adapter to bring the camera focal plane into alignment with the field of view. Each lens aperture was set to $f\# = 8$ to maximize the depth of field. A 4.00 cm thick light sheet was used to illuminate the measurement volume using a 150 mJ/pulse Quantel EverGreen HP, Nd:YAG laser. The data were recorded in double frame camera mode with $dt_{image} = 19.00$ ms at an acquisition frequency of 1.00 Hz. Tomographic PIV data were only acquired over the time-span of the interaction ranging from 8.00 to 30.00 s. The water tank was seeded with the same particles as the 2D-PIV measurements (Cospheric fluorescent red polyethylene micro-spheres (995 kg m^{-3}) particles with a diameter of 65–75 μm).

Image pre-processing was performed in DaVis 10.02.01 to eliminate background noise and compensate for intensity differences between images. A 5×5 pixel sliding minimum convolution filter was first applied. All images were then normalized with a reference image (the first image of each set), and a 5×5 pixel Gaussian filter was then used to sharpen the image. Volume-self-calibration routines were performed with DaVis 10.02.01 software to generate a mapping function between image coordinates and physical volume coordinates. The final volume self-calibration error had an average disparity of 0.06 voxel and a maximum disparity of 0.23 voxel. After image prepossessing and particle image volume reconstruction via the multiplicative algebraic reconstruction technique (MART), a multi-pass cross correlation technique was employed decreasing the interrogation volume from $128 \times 128 \times 128$ pixel to $32 \times 32 \times 32$ pixel with an overlap between adjacent interrogation regions of 50%. The final measurement volume was $1.50 \times 7.00 \times 4.00$ cm^3. The spatial resolution of the tomo-PIV data was 0.19 cm in all axes. The uncertainty in the tomo-PIV measurements was estimated using the tomographic uncertainty analysis technique available in the DaVis software. The uncertainty values were found to be $U_z = 1.25\%$, $U_{r_l} = 1.05\%$, and $U_{r_t} = 3.35\%$. The out-of-plane component had higher uncertainty due to the lower resolution and sensitivity of the reconstruction process in this direction.

C. Data analysis and validation

The λ_2-criterion[45] was employed to identify the vortex ring core location and the associated trajectories throughout the interaction. The instantaneous circulation (Γ) of each vortex ring was computed as the area integral of the vorticity over the bounds of the largest closed contour of vorticity that was within 65% of the maximum value of vorticity in the core. This value was chosen to ensure a closed contour of vorticity, over which the circulation and core area were computed, could be identified for the PVR, SVR, and TVR through the entirety of the interaction. The corresponding value of the cross-sectional area of the vortex core was expressed as πR_c^2, where R_c is the equivalent core radius. For each case (i.e., value of γ) the vorticity plots were nondimensionalized as $\omega^* = \omega/(\Gamma_{max,PVR}/\pi R_c^2)$, where $\Gamma_{max,PVR}$ is the peak circulation of the PVR for the case of interest, which was computed after the vortex ring was fully formed (i.e., the circulation reached a steady value). More details regarding the dynamics of the generated vortex ring are available in prior work.[31]

To ensure repeatability of the vortex ring generation the distribution of the vorticity along a line bisecting the core of the PVR is presented in Fig. 5 at time $\tau = 5.04$ for all of the investigated cases. The distribution of the vorticity, ω, is plotted as a function of the normalized transverse distance ($r^* = r/d_t$). Both the symmetry in the vorticity distribution and repeatability across all cases indicates robustness in the generation of the vortex ring.

The experimental facility was also validated by comparing the dynamics produced by a vortex ring impinging on a flat plate with the existing literature.[14,27,42] Excellent agreement was found; the details of which can be found in prior work.[31]

III. RESULTS

The flow physics of a vortex ring impacting a concave cavity, and the influence of cavity diameter (i.e., γ) on this behavior, is reported herein. Emphasis is placed on identifying how the formation and dynamics of the SVR is influenced by γ.
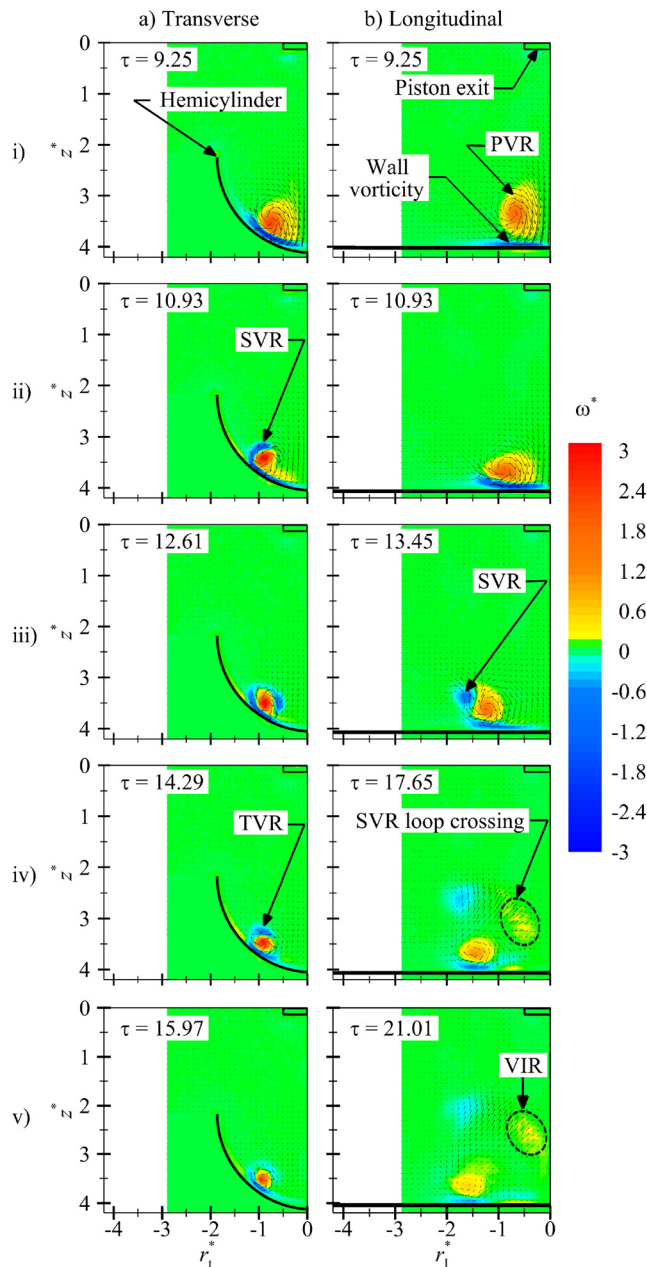
A. Primary physics of interaction

The primary physics produced by a vortex ring impinging on a hemicylindrical cavity are initially discussed for the case of $\gamma = 3$.
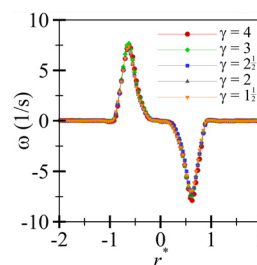
FIG. 5. Vorticity distribution along a line bisecting the center of the primary vortex ring core.

Figure 6 (multimedia available online) presents 2D-PIV data as vorticity plots with velocity vectors overlaid at five instances in the transverse [Fig. 6(a)] and longitudinal [Fig. 6(b)] planes. Note that when comparing Figs. 6(a) and 6(b), the non-dimensional times at which the data are reported are different. These discrepancies are intentional as the
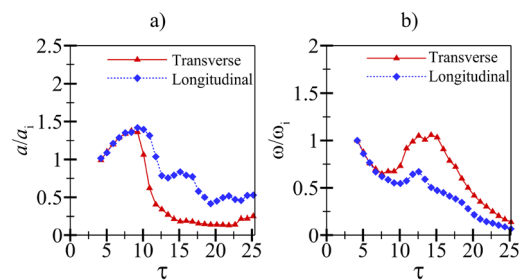
key flow physics occur at different instances in time in the two planes. Figure 7 represents the temporal variation of the (a) the core area, and (b) the peak core vorticity of the PVR in the transverse and longitudinal planes. The core area and peak core vorticity are normalized by their initial values, which correspond to the time at which the vortex ring becomes fully formed ($\tau = 4.2$). The core area, as opposed to the diameter, is chosen because the shape of the PVR core continuously changes throughout the interaction. As the PVR approaches the bottom of the hemicylinder a sheet of opposite sign vorticity is generated on the hemicylinder surface due to the no slip condition at the wall. This occurs in both the transverse and longitudinal planes, as evidenced in Fig. 6(i). Due to the curvature of the hemicylinder, the PVR first impacts the wall of the hemicylinder in the transverse plane before impacting the trough of the hemicylinder in the longitudinal plane.

Due to the asymmetric impact of the PVR on the hemicylindrical cavity surface, the PVR experiences non-uniform stretching, similar to the phenomenon observed for a vortex ring impinging on an obliquely oriented flat plate.[32] The segments of the PVR that impact the hemicylinder wall in the transverse plane undergo higher stretching than the segments of the PVR in the longitudinal plane. Due to this nonuniform stretching post impact ($\tau > 9.25$) the core area decreases in both planes, with the transverse plane showing a much greater reduction in area [see Fig. 7(a)]. This smaller area corresponds with increased peak vorticity in the core. Post impact ($\tau > 9.25$) the peak vorticity increases in both planes, but it is much more pronounced in the transverse plane, indicating increased rotational speed of the PVR [see Fig. 7(b)]. This difference in vorticity distribution between the transverse and longitudinal planes is expected to initiate bi-helical vortex lines around the circumference of the PVR that propagate from the transverse to longitudinal plane, as explained by Lim.[32] Unfortunately, the resolution of the acquired data was not sufficient to visually observe the formation of bi-helical vortex lines.

Asymmetric collision between the PVR and the cavity surface produces an asymmetric secondary vortex ring (SVR). The SVR first forms in the transverse plane before forming in the longitudinal plane as the PVR continues to translate down/toward the trough of the hemicylinder [see Fig. 6(ii–iii)]. Earlier generation of the SVR in the transverse plane produces a circumferential flow along the PVR core from the transverse plane to the longitudinal plane, this flow compresses the bi-helical vorticity toward the longitudinal plane. As a result,
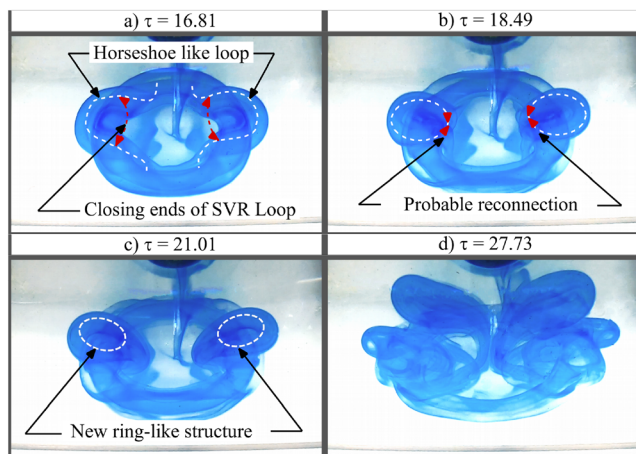

FIG. 6. Vorticity contours with velocity vectors overlaid for an axisymmetric vortex ring with $Re_\Gamma = 1500$ impacting a hemicylindrical cavity of $\gamma = 3$. Data are presented in the (a) transverse plane and (b) longitudinal plane. VIR (Vortex interaction region) identifies the region where the SVR loops interact. Multimedia available online.

FIG. 7. Temporal variation of the (a) core area and (b) peak core vorticity, of the PVR in the transverse and longitudinal planes for a $Re_\Gamma = 1500$ axisymmetric vortex ring impacting a $\gamma = 3$ hemicylindrical cavity. The cross-sectional area (a) of the PVR core is normalized by the initial core area (a_i), and the peak core vorticity (ω) is normalized by maximum peak core vorticity (ω_i).

immediately following contact at $\tau = 13.45$, the area of the PVR core in the longitudinal plane briefly increases [see Fig. 7(a)].

After the SVR is formed it orbits around the PVR due to mutual induction between them. The non-uniform vorticity distribution along the PVR core combined with the change in area between the transverse and longitudinal planes results in non-uniform rotation of the SVR around the PVR. The segments of the SVR closest to the transverse plane rotate faster than the segments closest to the longitudinal plane [see Fig. 6(ii–iii)]. As a result, the PVR and SVR become intertwined with the SVR segments closest to the transverse plane completely orbiting around the PVR [see Fig. 6(a)(ii–iv)]. In contrast, in the longitudinal plane the SVR does not completely orbit the PVR. A tertiary vortex ring (TVR) is also generated in the transverse plane at $\tau = 14.29$ [see Figure 5(a)(iv)]. The TVR orbits the PVR in the transverse plane in a manner similar to the SVR [see Fig. 6(a)(iv–v)].

Due to the increased diameter of the PVR in the longitudinal plane the SVR rotates around the PVR core with a larger arc. Moreover, the angular velocity of the PVR in the longitudinal plane is less than the transverse plane. Together, these result in a decreased orbital rotational velocity of the SVR in the longitudinal plane. The difference in rotational velocity between the transverse and longitudinal planes, which causes the PVR and SVR to become intertwined, introduces kinking in the SVR toward the extents of the PVR that align with the longitudinal plane. This can clearly be seen in the flow visualization images from the top view, which are presented in Fig. 8 (multimedia available online) at four instances in time during the interaction. As the kinking becomes more pronounced, the extents of the SVR form horseshoe-like loop vortices at each end [see Fig. 8(a)]. As the interaction progresses, the legs of the horseshoe loop approach each other while orbiting around the PVR [see Fig. 8(b)]. If sufficiently close in proximity, the legs can experience reconnection such that two new vortex rings are formed at the extents of the longitudinal plane [see Fig. 8(c)]. These newly formed vortex rings subsequently self-advect upward and away from the trough of the hemicylindrical cavity [see Fig. 8(d)].
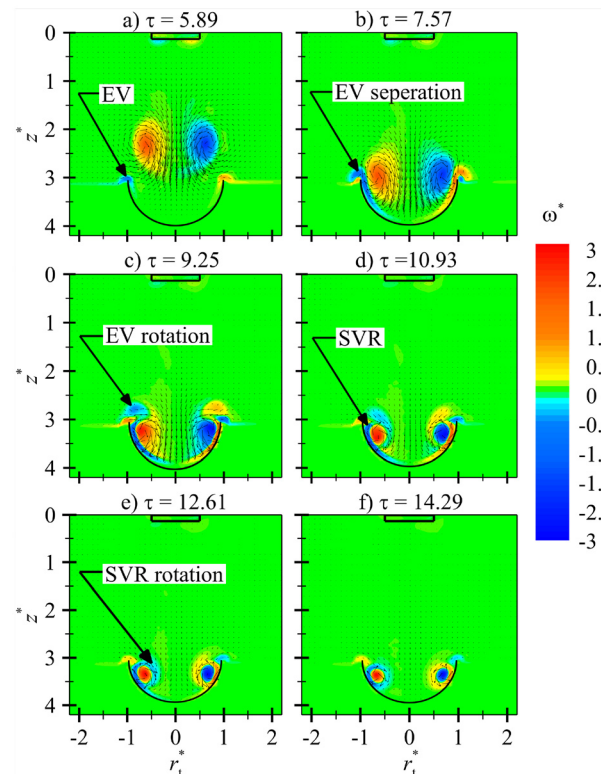
In Fig. 6(b)(iv–v), the probable reconnection of the legs of the horseshoe-like loop is also observed. Because it remains unclear whether complete reconnection between the loop legs occurs, this region is referred to as the vortex interaction region (VIR). This is because the legs of the horseshoe-like vortex interact in this region, as shown in Fig. 6(b)(v), This notation, VIR, will be employed throughout the remainder of the document to denote this region.

B. Influence of cavity size

Across the five considered cases ($\gamma = 4$, 3, $2\frac{1}{2}$, 2, and $1\frac{1}{2}$), four of them ($\gamma = 4$, 3, $2\frac{1}{2}$, 2, and $1\frac{1}{2}$) exhibited flow behavior in the transverse plane similar to that which has already been discussed for $\gamma = 3$. However, the smallest case ($\gamma = 1\frac{1}{2}$) exhibited marked changes. For this case, when the PVR approaches the cavity, it generates opposite sign vorticity along the edges of the cavity due to the similar size of the vortex ring and the cavity. This is shown in Fig. 9 (multimedia available online), which presents the vorticity contours and vector fields from the PIV data in the transverse plane at discrete instances in time throughout the interaction. The edge vorticity, referred to as EV in Fig. 9(a), intensifies as the PVR moves closer to the cavity. Simultaneously, a vorticity sheet is generated on the inner wall of the cavity [see Fig. 9(b)]. When the PVR passes the lip of the hemicylinder the edge vorticity separates from the lip due to the down-wash of the PVR. This, in turn, generates small scale, opposite sign vorticity at the

FIG. 8. Dye visualization from the inclined top view of a $Re_\Gamma = 1500$ axisymmetric vortex ring impacting on a hemicylindrical cavity with $\gamma = 3$. Multimedia available online.

FIG. 9. Vorticity contours with velocity vectors overlaid for an axisymmetric vortex ring with $Re_\Gamma = 1500$ impacting a hemicylindrical cavity of $\gamma = 1\frac{1}{2}$ at six instances in time. Data are presented in the transverse plane. Multimedia available online.
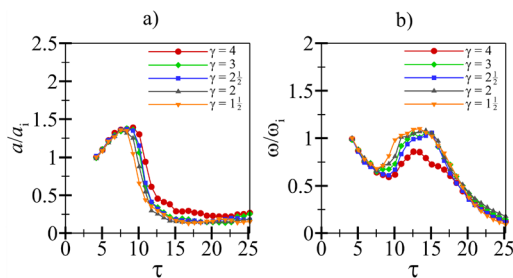
cavity edge [see Fig. 9(c)], while the separated EV rotates around the PVR due to mutual induction with the PVR [see Figs. 9(c) and 9(d)]. The PVR impacts the inner wall of the cavity close to the edge, during which the wall-bounded vorticity separates and rolls up into an SVR, as seen in Fig. 9(d). This then rotates around the PVR [see Fig. 9(e)] and, due to their proximity and having the same sense of rotation, the SVR and EV then merge as they orbit the PVR [see Fig. 9(f)]. The rest of the interaction then progresses the same as for the other cases of γ.

The transfer of vorticity from the transverse plane to the longitudinal plane due to the production of the circumferential flow along the core of the PVR occurred for all of the five cases considered. Figure 10 presents the change in time of the nondimensionalized area and core vorticity of the PVR in the transverse plane as a function of γ, while Fig. 11 presents the same data in the longitudinal plane. The trend of the PVR core area decreasing in the transverse plane, as previously discussed, was similarly observed for all values of γ, as shown in Fig. 10(a). In contrast, Fig. 11(a) shows that in the longitudinal plane the PVR core area initially decreases before increasing following the impact of the PVR on the trough of the cavity surface. Following impact of the PVR in the transverse plane, the maximum value of peak vorticity increases for decreasing γ. This can be seen in Fig. 10(b), when $10.09 \leq \tau \leq 13.45$. As previously discussed, this occurs because the PVR impacts the cavity surface earlier/higher up on the hemicylindrical cavity surface in the transverse plane, relative to the longitudinal plane. This generates increased stretching of the PVR and leads to higher vorticity in the transverse plane, relative to the longitudinal plane. This can be observed by comparing the magnitude of the vorticity in Fig. 10(b) with Fig. 11(b).

Along the longitudinal plane there are interesting changes to the physics of interaction as a function of hemicylindrical cavity size (γ). As previously discussed, asymmetric winding of the SVR around the PVR leads to kinking in the SVR and the formation of a horseshoe-like loop at the extents aligned with the longitudinal [see Fig. 8(a)]. This horseshoe-like loop then advects up and away from the trough of the cavity. To explore this behavior, Fig. 12(a) (multimedia available online) presents vorticity contour plots at time $\tau = 25.21$ as a function of γ. Figure 12(b) plots the location in time of the PVR, SVR, TVR, and VIR for the same values of γ.

For $\gamma = 4$ [Figs. 12(a)(i) and 12(b)(i)], the SVR forms a horseshoe-like loop at the extents of the longitudinal plane, similar to
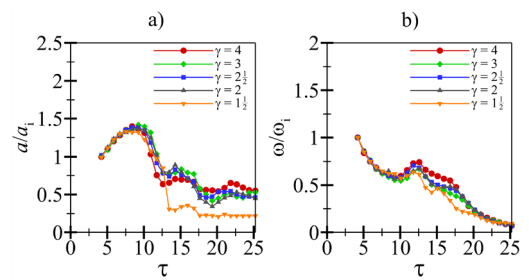
FIG. 11. Temporal variation of the PVR (a) core area and (b) peak core vorticity, in the longitudinal plane for a $Re_\Gamma = 1500$ axisymmetric vortex ring impacting five hemicylindrical cavities of $\gamma = 4$, 3, $2\frac{1}{2}$, 2, & $1\frac{1}{2}$. The cross-sectional area (a) of the PVR core is normalized by the initial core area (a_i), and the peak core vorticity (ω) is normalized by maximum peak core vorticity (ω_i).
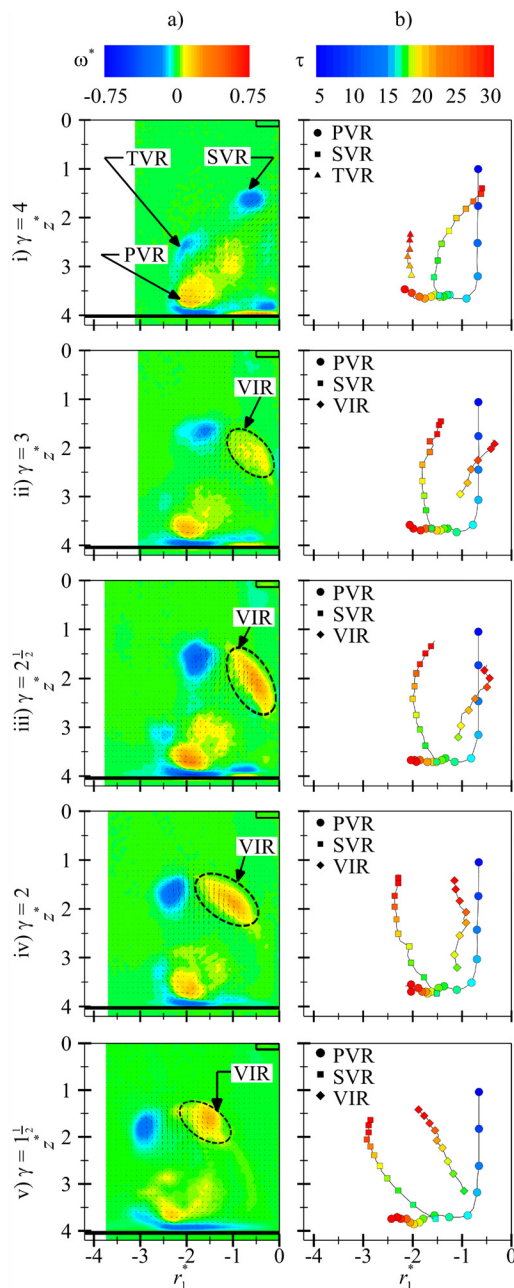
what was discussed and shown in Fig. 8(a), for $\gamma = 3$ [see also Figs. 12(a)(ii) and 12(b)(ii)]. However, for $\gamma = 4$, the legs of the horseshoe-like loop never cross the longitudinal plane or reconnect with each other. This is because the confinement of the PVR in the transverse plane is lowest for the largest case of $\gamma = 4$. Consequently, the asymmetry of impact, circumferential flow from the transverse to the longitudinal plane, and asymmetry in the peak core vorticity of the PVR, are all reduced (see Figs. 10 and 11). That is to say, its behavior begins to resemble that of a vortex ring impinging on a flat plate, where asymmetry in the SVR is minimized, as would occur as γ approaches infinity.[15,17]

Consequently, when $\gamma = 4$ the legs of the horseshoe-like loop come into close proximity, but do not reconnect, and mutual induction between them determines the trajectory of the ejected horseshoe vortex. This can be seen in the trajectory plots of Fig. 12(b)(i), where the primary direction is toward the axis of the PVR. Before forming a horseshoe-like vortex and being ejected away from the PVR, the SVR rotates a finite arc length around the PVR due to mutual interaction. This rotation of the SVR around the PVR produces a slight rebound in the trajectory of the PVR, as seen in Fig. 12(b)(i). Due to this rebound of the PVR a TVR is also generated and moves upward and away from the region of impact [see Fig. 12(b)(i)].

For all other cases [$\gamma = 3$, $2\frac{1}{2}$, 2, and $1\frac{1}{2}$, which correspond to figure panels 12(ii), 12(iii), 12(iv), and 12(v), respectively], the open ends of the horseshoe-like loops of the SVR interacts at the longitudinal plane and a ring-like structure is produced. This is observed in Figure 12(ii–v) as two regions of opposite-sign vorticity in the longitudinal plane, where the SVR is denoted, and the VIR is also identified. The VIR moves in tandem with the upward movement of the SVR. From the 2D longitudinal plane data, it appears that the SVR core and VIR form a closed loop that produces a new vortex ring.

However, the VIR will appear in the 2D-PIV flow domain as long as one of the legs of the horseshoe-like loop crosses the longitudinal plane (i.e., the data plane). This does not, however, definitely determine the formation of a new coherent vortex ring due to reconnection.

To determine whether reconnection occurs or not, tomo-PIV data were acquired for the cases of $\gamma = 3$, 2, & $1\frac{1}{2}$, and are plotted in Fig. 13 (multimedia available online) as iso-contours of the λ_2 criterion. The interaction at three different instances in time are presented in Fig. 13. Figure 13(a)(i) is presented at $\tau = 14.29$, when the horseshoe-like loop has been generated and is rotating around the

FIG. 10. Temporal variation of the PVR (a) core area and (b) peak core vorticity, in the transverse plane for a $Re_\Gamma = 1500$ axisymmetric vortex ring impacting five hemicylindrical cavities of $\gamma = 4$, 3, $2\frac{1}{2}$, 2, & $1\frac{1}{2}$. The cross-sectional area (a) of the PVR core is normalized by the initial core area (a_i), and the peak core vorticity (ω) is normalized by maximum peak core vorticity (ω_i).

FIG. 12. (a) Vorticity contours with velocity vectors overlaid for an axisymmetric vortex ring with $Re_\Gamma = 1500$ impacting a hemicylindrical cavity for $\gamma = 4, 3, 2\frac{1}{2}, 2$, and $1\frac{1}{2}$ at time $\tau = 20.10$. (b) The location of the PVR (circle), SVR (square), and RR (diamond) core plotted as a function of time, τ for the same values of γ. Multimedia available online.

PVR. For $\gamma = 3$, it can be seen that the legs of the horseshoe vortex do not approach each other as they orbit the PVR [see Fig. 13(a)(i–iii)] and do not appear to cross the longitudinal plane.

For $\gamma = 2 \& 1\frac{1}{2}$, the legs of the horseshoe-like loop are much closer to each other than for $\gamma = 3$ [see Figs. 13(b)(i) and 13(c)(i)].

Consequently, as the interaction progresses in time the legs of the horseshoe-like loop reconnect with each other [see Figs. 13(b)(ii–iii) and 13(c)(ii–iii)], and a new vortex ring is generated at both extents of the SVR in the longitudinal plane. Note that for the last instance in time [Fig. 13(iii)] only the SVR is presented (the PVR has been removed from the plot) to more easily visualize reconnection.

Due to instabilities that arise during the interaction, as well as the potential for experimental uncertainties in the production of the PVR, slightly off-axis collisions on the hemicylinder surface can occur. As a result, the legs of the horseshoe-like loop structures may not be perfectly symmetric about the longitudinal plane [see Fig. 13(i)]. This highlights the need to exercise care when interpreting 2D-PIV data, as slight shifts in the location of the legs of the horseshoe-like loop can result in them being bisected by the 2D PIV data in the longitudinal plane, which results in two regions of circular, opposite-sign vorticity appearing. This can easily be misinterpreted as a coherent vortex ring. In contrast, the tomographic PIV data of Fig. 13 clearly shows that reconnection only occurs for values of $\gamma \le 2$, which is when the kinking of the SVR is extreme enough that the legs of the horseshoe-like loop come into contact.

To investigate the production of the new vortex rings, the circulation strength of the SVR core and RR regions were compared at the time of formation. According to Morris *et al.*,[36] 2D-PIV data of a fully formed vortex ring should have the same circulation strength at both ends. Figure 14 shows how the circulation of the SVR and VIR vary in time throughout the interaction. For $\gamma = 3$ and $2\frac{1}{2}$ the circulation strength of the VIR never reaches the magnitude of that found in the SVR core [see Figs. 14(a) and 14(b)]. However, when $\gamma \le 2$ the magnitude of the circulation in both the VIR and SVR core ultimately equalize, confirming reconnection of the legs of the horseshoe-like loop and the subsequent formation of a new vortex ring. These data also clearly show that reconnection occurs earlier for decreasing values of γ, with it occurring at $\approx \tau = 24.3$ for $\gamma = 2$, and at $\approx \tau = 17.65$ for $\gamma = 1\frac{1}{2}$.

Returning to Fig. 12(b), it is notable that the trajectory of the SVR and VIR varies significantly as a function of γ. For $\gamma = 3$ and $2\frac{1}{2}$, the SVR and VIR advect toward the centerline of the PVR [see Fig. 12b(ii–iii)]. As γ decreases, the trajectory of the SVR and VIR becomes vertical and then moves away from the centerline of the PVR for smaller values [see Fig. 12b(iv–v)].

The explanation for this change in trajectory lies in the asymmetric impact of the PVR on the concave cavity surface. To explain this behavior Fig. 15(a) illustrates the difference in vertical distance (Δh) that the PVR must travel to impact the surface along the longitudinal plane compared to the transverse plane. As γ decreases the hemicylinder radius decreases, leading to an increase in Δh. Consequently, the delay in time between when the PVR impacts the hemicylinder surface in the transverse plane vs when it impacts the surface in the longitudinal plane, referred to as $\Delta \tau$, increases. This time delay was computed, and is shown in Fig. 15(b) as a function of γ. Impact of the vortex ring on the surface was determined as the time when the fluid velocity at the surface reached a maximum value. A fundamental observation of vortex ring–structure interactions is that when the vortex ring approaches a surface the vortex ring diameter increases.[14,15] As previously discussed, the wall curvature constrains the PVR in the transverse direction resulting in a reduced diameter in the transverse direction relative to the longitudinal direction. This is shown schematically in Fig. 15(c), where the blue ring represents the PVR and the red
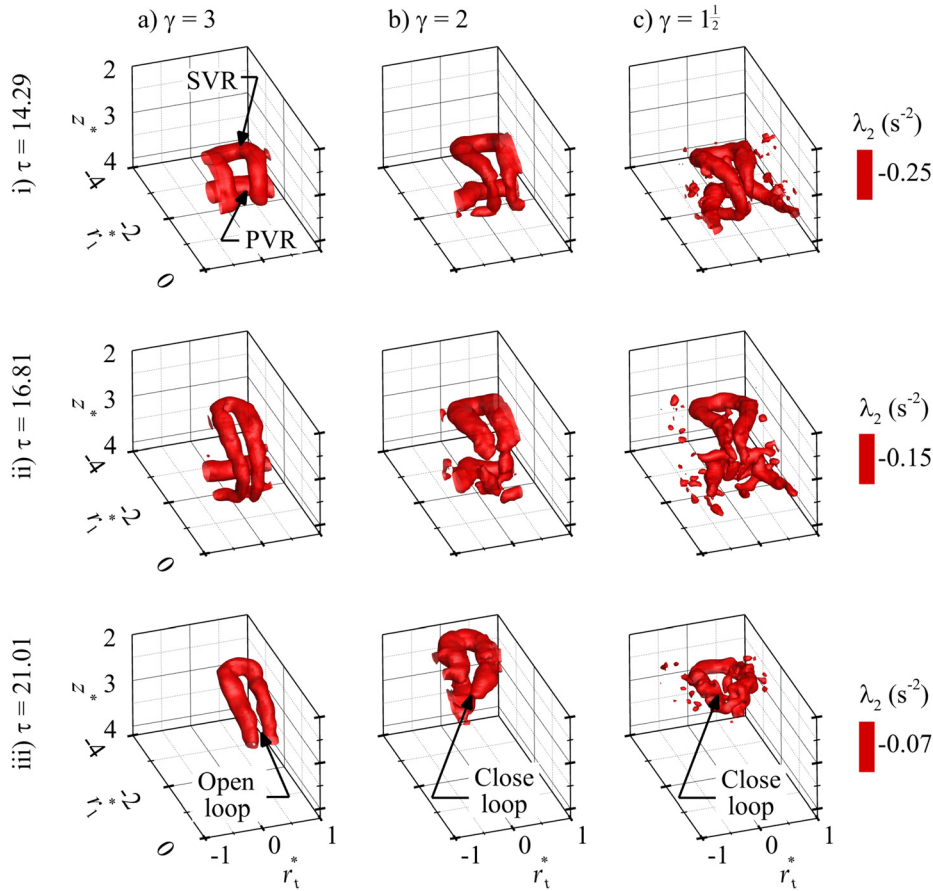
FIG. 13. Iso-contours of λ_2 (s^{-2}) criterion for an axisymmetric vortex ring with $Re_\Gamma = 1500$ interacting with a hemicylinder for (a) $\gamma = 3$, (b) $\gamma = 2$, and (c) $\gamma = 1\frac{1}{2}$, at three instances in time: (i) $\tau = 10.72$, (ii) $\tau = 16.08$, and (iii) $\tau = 17.42$. Multimedia available online.

ring represents the SVR. The major and minor axes of the PVR are expressed as $D_{\mathrm{PVR,major}}$ and $D_{\mathrm{PVR,minor}}$, respectively. Thus, as γ decreases the minor axis of the PVR decreases and the legs of the horseshoe-like loop structure come into increasingly closer contact. This leads to VIR occurring earlier as well, as shown in Fig. 12(b)(ii–v) and Fig. 14. In addition, the arc length that the SVR has to transcribe as it rotates around the PVR increases as γ decreases, because of the larger diameter, $D_{\mathrm{PVR,major}}$, of the PVR. Consequently, as γ decreases the outboard portion of the SVR core has not rotated as far around the PVR when either mutual induction between the legs of the horseshoe-like loop structure ($\gamma > 2$), or self-advection of the new vortex ring ($\gamma \leq 2$), begins to eject the vorticity. As a result, the trajectory of the SVR transitions from pointing toward the centerline of the PVR to pointing away from it as γ decreases.

Consequently, changing the ratio of hemicylinder to vortex ring radius provides a method for controlling the trajectory of the ejected vorticity and, for sufficiently small values of γ, generating new vortex rings. This contributes unique insight into the class of interactions arising from vortex rings impinging on concave cavities, where prior work employing an axisymmetric hemispherical cavity also found that the strength of the secondary vorticity that was ejected away from the surface of contact could be controlled by adjusting the value of γ.[31]

The current results are of particular interest for the scenario of replacement speech via a tracheoesophageal prosthesis, as prior work has shown that as the flow passes through the prosthesis and into the esophagus, periodic vortex rings are produced and impinge on the posterior wall of the esophagus.[11] More importantly, clinical observations have found that simply changing the orientation of the prosthesis,
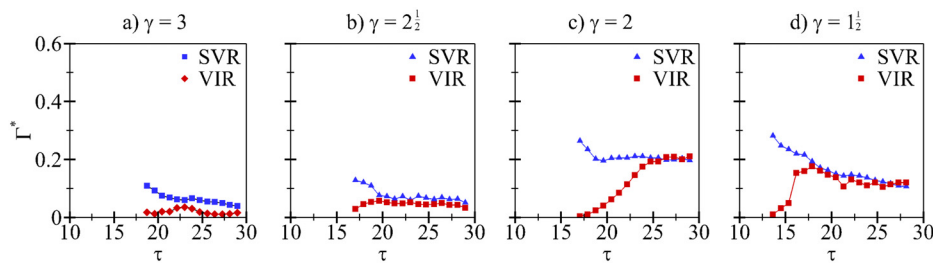
FIG. 14. Circulation as a function of time for the SVR and RR (a) $\gamma = 3$, (b) $\gamma = 2\frac{1}{2}$, (c) $\gamma = 2$, and (d) $\gamma = 1\frac{1}{2}$. The circulation is normalized by the maximum value of the PVR circulation ($\Gamma^* = \Gamma/\Gamma_{\mathrm{PVR,max}}$).
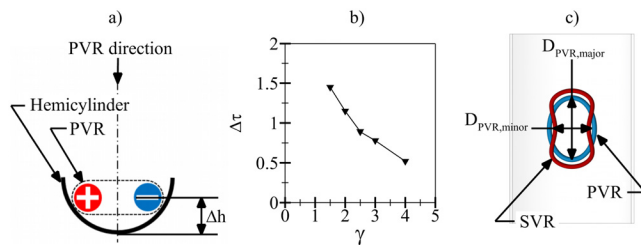
FIG. 15. (a) Schematic representation of the PVR impacting on the hemicylinder in the transverse plane, (b) the non-dimensionalized time difference ($\Delta\tau$) between vortex ring-surface impact in the longitudinal and transverse planes, and (c) a schematic representation of the stretching and subsequent asymmetry in the rotation of the SVR around the PVR.

FIG. 16. Schematic representation of SVR evolution for different cases.
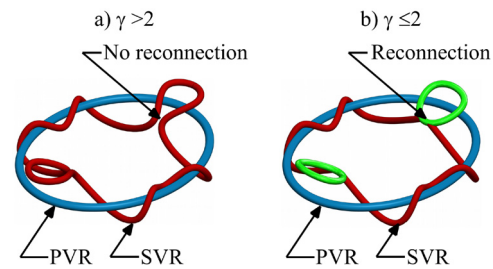
thereby altering the trajectory of the vortex ring as it enters the esophagus, often drastically improves, and can even completely restore, phonation in aphonic individuals.[38] The formation and trajectory of vortical structures throughout this interaction is then, of critical importance in determining the quality of replacement speech that can be produced via tracheoesophageal speech.

IV. CONCLUSION

In this study, the interaction arising from an axisymmetric vortex ring impinging on a hemicylindrical concave cavity was explored as a function of the ratio of hemicylindrical cavity to vortex ring radius ($\gamma = R_{\mathrm{cyl}}/R_{\mathrm{V}} = 4, 3, 2\frac{1}{2}, 2,$ and $1\frac{1}{2}$). This is an extension of prior work that investigated a vortex ring impacting a concave hemispherical cavity.[31] The results presented herein show similarities to prior work investigating an axisymmetric vortex ring impacting a constant radius, 2D concave hemicylindrical cavity as a function of Reynolds number,[39] and a 2D V-wall.[35] However, in the current work, comparing the dynamics in the transverse and longitudinal planes lead to the identification of new flow physics that arise due to changing the radius of the cavity relative to the primary vortex ring.

In the transverse plane, the flow behavior changed subtly but significantly as γ varies. Both SVR and TVR were generated and rotated around the PVR after it impacted the cavity surface. As γ decreased (indicating increased wall curvature), the PVR impacted the cavity wall earlier and at a higher location, leading to increased PVR stretching and vorticity diffusion. The greater stretching of the PVR facilitated the transfer of vorticity from the transverse to the longitudinal plane through its core, a process that intensifies with decreasing γ. Note that for the lowest value tested, $\gamma = 1\frac{1}{2}$, edge vorticity is formed on the lip of the cavity, rolls up, and rotates around the PVR.

In the longitudinal plane, the mechanics of formation and ejection of SVR were detailed, identifying how the trajectory of the ejected vorticity depends on the cavity size to vortex ring size ratio, γ. The PVR impacted the cavity surface in the transverse plane followed by impact in the longitudinal plane. Upon impact in the longitudinal plane, the PVR core initially decreased in diameter, then expanded due to circumferential flow and vorticity transfer from the transverse plane to the longitudinal plane. The rotation of the SVR around the PVR was slower in the longitudinal plane due to the larger PVR core diameter and reduced circulation, leading to the formation of horseshoe-like loops at each end of the SVR. Figure 16 schematically represents the evolution of the SVR horseshoe-like loops. For $\gamma > 2$, the SVR loops experienced mutual induction and moved away from the cavity surface [see Fig. 16(a)], and no reconnection between the loop legs occurred. For $\gamma \leq 2$, the loops reconnected to form a new vortex ring that also advected away from the surface [see Fig. 16(b)]. However, the trajectories varied as a function of γ transitioning from angling toward the centerline for $\gamma = 4$, to angling away from the centerline for $\gamma = 1\frac{1}{2}$. This arose due to the delay in time of PVR impact between the transverse and longitudinal planes.

These new findings have direct application to optimizing the fluid–structure interactions that occur within the esophagus during replacement speech produced by tracheoesophageal speech.

AUTHOR DECLARATIONS
Conflict of Interest

The authors have no conflicts to disclose.

Author Contributions

Tanvir Ahmed: Formal analysis (lead); Investigation (lead); Methodology (equal); Visualization (lead); Writing – original draft (lead); Writing – review & editing (equal). **Byron D. Erath:** Conceptualization (lead); Funding acquisition (lead); Methodology (equal); Project administration (lead); Supervision (lead); Writing – review & editing (equal).

DATA AVAILABILITY

The data that support the findings of this study are available from the corresponding author upon reasonable request.

REFERENCES

[1]C. Cornaro, A. Fleischer, and R. Goldstein, "Flow visualization of a round jet impinging on cylindrical surfaces," Exp. Therm. Fluid Sci. **20**, 66–78 (1999).

[2]K. Mohseni, "Pulsatile vortex generators for low-speed maneuvering of small underwater vehicles," Ocean Eng. **33**, 2209–2223 (2006).

[3]S. D. Peterson and M. Porfiri, "Energy exchange between a vortex ring and an ionic polymer metal composite," Appl. Phys. Lett. **100**, 114102 (2012).

[4]J. C. Hu, Y. Cha, M. Porfiri, and S. D. Peterson, "Energy harvesting from a vortex ring impinging on an annular ionic polymer metal composite," Smart Mater. Struct. **23**, 074014 (2014).

[5]A. Pirnia, J. C. Hu, S. D. Peterson, and B. D. Erath, "Vortex dynamics and flow-induced vibrations arising from a vortex ring passing tangentially over a flexible plate," J. Appl. Phys. **122**, 164901 (2017).

[6]A. Pirnia, S. D. Peterson, and B. D. Erath, "Temporal response of a flexible cantilevered plate subjected to tangentially-advecting vortex rings: Application to energy harvesting systems," J. Fluids Stru. **103**, 103284 (2021).

[7]C. Gong, Y. Cheng, and Y. Jiang, "Investigation into fresh air delivery performance with vortex ring," Sci. Total Environ. **885**, 163874 (2023).

[8]R. Faludi, M. Szulik, J. D'hooge, P. Herijgers, F. Rademakers, G. Pedrizzetti, and J. Voigt, "Left ventricular flow patterns in healthy subjects and patients with prosthetic mitral valves: An in vivo study using echocardiographic particle image velocimetry," J. Thorac. Cardiovasc. Surg. **139**, 1501–1510 (2010).

[9]M. Markl, P. J. Kilner, and T. Ebbers, "Comprehensive 4d velocity mapping of the heart and great vessels by cardiovascular magnetic resonance," J. Cardiovasc. Magn. Reson. **13**(1–22), 7 (2011).

[10]K. Kamemoto and A. Ojima, "Application of a vortex method to fluid dynamics in sports science," in *Fluids Engineering Division Summer Meeting* (ASME, 2007), Vol. 42886, pp. 1051–1060.

[11]B. D. Erath and F. S. Hemsing, "Esophageal aerodynamics in an idealized experimental model of tracheoesophageal speech," Exp. Fluids. **57**, 34 (2016).

[12]T. B. Le, M. S. Elbaz, R. J. V. D. Geest, and F. Sotiropoulos, "High resolution simulation of diastolic left ventricular hemodynamics guided by four-dimensional flow magnetic resonance imaging data," Flow. Turbul. Combust. **102**, 3–26 (2019).

[13]U. Boldes and J. C. Ferreri, "Behavior of vortex rings in the vicinity of a wall," Phys. Fluids **16**, 2005–2006 (1973).

[14]J. D. A. Walker, C. R. Smith, A. W. Cerra, and T. L. Doligalski, "The impact of a vortex ring on a wall," J. Fluid Mech. **181**, 99–140 (1987).

[15]A. W. Cerra, "Experimental observations of vortex ring interaction with the fluid adjacent to a surface," Ph.D. thesis (Lehigh University, 1983).

[16]C. C. Chu, C. T. Wang, and C. C. Chang, "A vortex ring impinging on a solid plane surface—vortex structure and surface force," Phys. Fluids. **7**, 1391–1401 (1995).

[17]P. Orlandi and R. Verzicco, "Vortex rings impinging on walls: Axisymmetric and three-dimensional simulations," J. Fluid Mech. **256**, 615–646 (1993).

[18]I. Danaila, "Vortex dipoles impinging on finite aspect ratio rectangular obstacles," Flow Turbul. Combust. **72**, 391–406 (2004).

[19]J. O. Dabiri, S. P. Colin, J. H. Costello, and M. Gharib, "Flow patterns generated by oblate medusan jellyfish: Field measurements and laboratory analyses," J. Exp. Biol. **208**, 1257–1265 (2005).

[20]M. Cheng, J. Lou, and L. S. Luo, "Numerical study of a vortex ring impacting a flat wall," J. Fluid Mech. **660**, 430–455 (2010).

[21]J. T. Hrynuk, V. J. Luipen, and D. Bohl, "Flow visualization of a vortex ring interaction with porous surfaces," Phys. Fluids. **24**, 037103 (2012).

[22]B. J. Gemmell, J. H. Costello, S. P. Colin, C. J. Stewart, J. O. Dabiri, D. Tafti, and S. Priya, "Passive energy recapture in jellyfish contributes to propulsive advantage over other metazoans," Proc. Natl Acad. Sci. USA **110**, 17904–17909 (2013).

[23]T. T. Lim and D. Adhikari, "The impact of a vortex ring on porous surfaces—a review," in *Vortex Rings Jets* (Springer, 2015), pp. 33–60.

[24]Q. Li and C. H. Bruecker, "Vortex interaction with a rough wall formed by a hexagonal lattice of posts," Phys. Fluids **30**, 054107 (2018).

[25]M. Samaee, "Vortex ring propagation in confined spheroidal domains and applications to cardiac flows," Ph.D. thesis (Oklahoma State University, 2019).

[26]A. J. Peace and N. Riley, "A viscous vortex pair in ground effect," J. Fluid Mech. **129**, 409–426 (1983).

[27]R. Verzicco and P. Orlandi, "Wall/vortex-ring interactions," Appl. Mech. Rev **49**(10), 447 (1996).

[28]R. Verzicco and P. Orlandi, "Normal and oblique collisions of a vortex ring with a wall," Meccanica **29**, 383–391 (1994).

[29]T. L. Doligalski, C. R. Smith, and J. D. A. Walker, "Vortex interactions with walls," Annu. Rev. Fluid Mech. **26**, 573–616 (1994).

[30]J. K. Harvey and F. J. Perry, "Flowfield produced by trailing vortices in the vicinity of the ground," AIAA J. **9**, 1659–1660 (1971).

[31]T. Ahmed and B. D. Erath, "Experimental study of vortex ring impingement on concave hemispherical cavities," J. Fluid Mech. **967**, A38 (2023).

[32]T. T. Lim, "An experimental study of a vortex ring interacting with an inclined wall," Exp. Fluids **7**, 453–463 (1989).

[33]L. D. Couch and P. S. Krueger, "Experimental investigation of vortex rings impinging on inclined surfaces," Exp. Fluids **51**, 1123–1138 (2011).

[34]T. H. New, S. Shi, and B. Zang, "Some observations on vortex-ring collisions upon inclined surfaces," Exp. Fluids **57**, 109 (2016).

[35]T. H. New, B. Zang, J. Long, and S. Shi, "Collision of vortex rings upon v-walls," J. Fluid Mech. **899**, A2 (2020).

[36]S. E. Morris and C. H. K. Williamson, "Impingement of a counter-rotating vortex pair on a wavy wall," J. Fluid Mech. **895**, A25 (2020).

[37]F. L. Sotiropoulos, B. Trung, and A. Gilmanov, "Fluid mechanics of heart valves and their replacements," Annu. Rev. Fluid Mech. **48**, 259–283 (2016).

[38]C. K. Oh, R. J. Meleca, M. L. Simpson, and J. P. Dworkin, "Fiberoptic examination of the pharyngoesophageal segment in tracheoesophageal speakers," Arch. Otolaryngol. Head Neck Surg. **128**, 692–697 (2002).

[39]L. Zhang, G. Li, W. L. Chen, and D. Gao, "Reynolds number effect of a vortex ring impinging on a concave hemi-cylindrical shell," Phys. Fluids. **36**, 075140 (2024).

[40]M. Gharib, E. Rambod, and K. Shariff, "A universal time scale for vortex ring formation," J. Fluid Mech. **360**, 121–140 (1998).

[41]N. Didden, "On the formation of vortex rings: Rolling-up and production of circulation," J. Appl. Math. Phys. (ZAMP) **30**, 101–116 (1979).

[42]M. Shusser, M. Rosenfeld, J. O. Dabiri, and M. Gharib, "Effect of time-dependent piston velocity program on vortex ring formation in a piston/cylinder arrangement," Phys. Fluids. **18**, 033601 (2006).

[43]R. P. Dring, "Sizing criteria for laser anemometry particles," J. Fluids Eng. **104**, 15–17 (1982).

[44]A. Sciacchitano and B. Wieneke, "Piv uncertainty propagation," Meas. Sci. Technol. **27**, 084006 (2016).

[45]J. Jeong and F. Hussain, "On the identification of a vortex," J. Fluid Mech. **285**, 69–94 (1995).